Composites Part B 247 (2022) 110352

Contents lists available at ScienceDirect

Composites Part B

journal homepage: www.elsevier.com/locate/compositesb

3D-printed in-line and out-of-plane layers with stimuli-responsive intelligence

Dharneedar Ravichandran [a], Mounika Kakarla [b], Weiheng Xu [a], Sayli Jambhulkar [a], Yuxiang Zhu [a], Mohammed Bawareth [c], Nathan Fonseca [c], Dhanush Patil [a], Kenan Song [d,*]

[a] *Systems Engineering, School of Manufacturing Systems and Networks, Ira A. Fulton Schools of Engineering, Arizona State University, Mesa, AZ, 85212, USA*
[b] *Materials Science and Engineering, The School of Engineering of Matter, Transport and Energy (SEMTE), Ira A. Fulton Schools of Engineering, Arizona State University, Tempe, AZ, 85281, USA*
[c] *Mechanical Systems Engineering, The Polytechnic School (TPS), Ira A. Fulton Schools for Engineering, Arizona State University, Mesa, AZ, 85212, USA*
[d] *The Polytechnic School (TPS), School of Manufacturing Systems and Networks (MSN), & the School of Engineering of Matter, Transport and Energy (SEMTE), Ira A. Fulton Schools of Engineering, Arizona State University, Mesa, AZ, 85212, USA*

ARTICLE INFO

Keywords:
3D printing
Thermoplastic polyurethane
Composites
Stimuli responsiveness
Shape memory effect

ABSTRACT

Smart materials and structures with shape memory properties have recently gained attention due to their unique ability to remember their original shape, dimensional flexibility, structural programmability, and multi-material compatibilities. They have found applications in morphing structures, heat storage, flexible electronics, soft/micro-robotics, metamaterials, biomedical scaffolds, and space missions. Most applications of these systems require multifunctionality with high precision controls over multi-materials. However, most current manufacturing cannot process disparate materials without generating phase separation or structural instabilities. This research presents a new 3D printing process via the Multiphase Direct Ink Writing (MDIW) mechanism to produce in-line and out-of-plane microlayers. The selective deposition of polyether-thermoplastic polyurethane (TPU)/polycaprolactone (PCL) and polyester-TPU/iron oxide (Fe_3O_4) is investigated for thermal and magnetic dual stimuli-responsiveness. During the MDIW manufacturing, specific sublayers within each printing line for optimized domain size are produced with the stacking of the layers along the z-axis to investigate their influences on the stimuli-responsiveness. The mechanical, thermal, and thermomechanical characterizations can reveal the time-temperature-dimension relationships in different media (i.e., air and water) showing a precisely controlled actuation phenomenon and shedding light on their broad applications in defense, energy, health, and sustainability.

1. Introduction

Polymers with stimuli-responsiveness (i.e., smart/intelligent polymers) can alter their physical and/or chemical properties upon exposure to specific environmental conditions. As a result, these materials have broad applications in sensors, actuators, soft robotics, innovative coatings, environmental remediation, targeted drug delivery, and tissue engineering [1–4]. Among these intelligent polymers, shape memory polymers (SMPs) have attracted attention due to their advantages in lightweight (i.e., 1–2 g/cm^3), mechanical robustness (e.g., extensive strain recovery), thermal manipulability (e.g., a wide range of glass transition temperatures), electrical insulation, chemical stability (e.g., corrosion resistance), biocompatibility, and low-cost processability [4–7]. In addition, the high sensitivity and selectivity to specific environmental parameters give SMPs highly flexible transformations between morphing geometry and initially designed dimensions. The external stimuli to tune SMPs' shapes and dimensions include mechanical loading, thermal heat, electrical field, optical light, magnetic field, and chemical pH [8–11]. However, the shape memory effect of the SMPs relies strictly on the active and passive phases to generate responsive behavior to respective external stimuli. The active phase is responsible for the temporary shape-shifting, and the passive phase is responsible for regaining the original shape. The chemical composition, physical variations, or structural differences between these phases generate stress variations that respond differently within a specific environment [12–14]. Copolymerization via monolayers, manual laminating, or

---

* Corresponding author.
E-mail address: Kenan.song@asu.edu (K. Song).

https://doi.org/10.1016/j.compositesb.2022.110352
Received 11 July 2022; Received in revised form 26 September 2022; Accepted 11 October 2022
Available online 15 October 2022

casting of bilayer or trilayer structures are commonly-utilized fabrication techniques for producing SMPs [15–18]. However, one limitation of these techniques is their difficulty in creating complex shapes of varying chemistry, compositions, dimensions, and topologies, in addition to the often criticized long lead time or high cost [19–22]. For example, Zhang et al. fabricated thermally responsive shape memory material through a multi-step process involving a series of processing methods, e.g., ultra-sonication, milling, hot pressing, and thermally induced aging, which limits the choices of materials or the fabrication precisions [23].

Additive manufacturing (i.e., 3D printing) is an effective technique for rapid prototyping and customized design. For example, 3D printing can deposit materials at user-defined positions and allow dimensional variation to provide desirable actuation control of complex geometries [24]. In addition, different printing mechanisms can include multi-materials at different scales [25]. Precisely, the selective laser sintering (SLS) disperses finer microspheres within coarse powders, the fused deposition modeling (FDM) mixes macroscale carbon fibers in the polymer matrix, direct ink writing (DIW) suspends micro ceramics in soft matter solutions or gels, and stereolithography (SLA) blends nanoparticles in monomer resins [26–29]. More importantly, the inclusion of stimuli-responsiveness in 3D printing can add one more dimensional control (i.e., time) to physical dimensions, leading to the newly defined 4D printing [30,31]. For example, JA Lewis and her group used DIW to 3D print shape morphing liquid crystal elastomers (LCEs) above and below its nematic-to-isotropic transition temperature when exposed to high-temperature UV light [32]. Similarly, HJ Qi and his group fabricated heat-responsive shape memory structures using shape memory polymer fibers and polyjet 3D printing technique [33]. The structural or composition evolutions as a function of time generate a new level of affordability and ease of use for unique applications in human implants (e.g., cell encapsulation or drug delivery), energy storage (e.g., heat dissipation and packaging reliability in extreme temperatures), actuators (e.g., hinge mechanism or lightweight load-bearing), and electronics (e.g., morphing electronics) [20,21,34–37]. Different 4D printing materials, including polymers, hydrogels, liquid crystal elastomers, ferromagnetic nanoparticles, carbon/ceramic nanoparticles, and bio-inks, have been reported in versatile structures [38–40]. However, most 4D printing feedstocks are phase-mixed i.e., simple mixing of two or more polymers or nanoparticles to produce shape memory actuation but may compromise its mechanical properties [41]. Therefore, it is urgent to develop an integrated manufacturing platform for selectively distributing multiple phases to respond to external stimuli in a programmable manner. Examples are multi-material inclusion instead of simple mixtures, new hierarchical designs at the mesoscale, high manufacturing scalability, and maneuverability in coupled fields via innovative protocols.

This research focuses on a newly developed multiphase direct ink writing (MDIW) 3D printing technique to print in-line and out-of-plane layered structures critical for stimuli-responsiveness via controlled heat or magnetism. The MDIW uses a nozzle specially designed to take multi-materials (e.g., gels containing different polymers and nanoparticles) as feedstocks before rearranging them alternatively in the multipliers, forming sub-layers within each printing line and enabling hierarchical in-plane and out-of-plane layers. These multi-materials include (i) polyether- and polyester-based thermoplastic polyurethane (TPU) elastomers for reversible shape morphing, (ii) polycaprolactone (PCL) for thermal actuation, and (iii) iron oxide (Fe_3O_4) for magnetic manipulations. In addition, the layer numbers can influence the thermal transition and actuation of the polymer composites, demonstrating their consistent effectiveness in expanding rolled structures with different heating temperatures, printing textures, and moisture degrees. Specifically, the layer number along with the in-plane (i.e., x/y-axis) was optimized to be 64 per printing line due to (i) distinct layer formation and (ii) uniform nanoparticle dispersions. Besides, the layer number along the out-of-plane (i.e., z-axis) varied from 3 to 10 (i.e., 3L–10L) to study the actuation tunability. Based on this structural design, the actuation mechanism was studied using the shape memory effect (SME) analysis by subjecting the samples to a repeated thermo-mechanical cycle with *in-situ* dynamic observations. Furthermore, thermal unbuckling of complex morphologies (i.e., multifold, cylindrical, and helix) and the magnetic rotation of fixed samples also showed the highly efficient stimuli-responsiveness useful for broad applications in sensors, actuators, and soft robotics.

2. Experimental

Materials: TPU-D (Ellastollan 1254 D 13 U) and TPU-B (Ellastollan B 60 A 10 WHTSG 000) were provided by BASF, USA. TPU-D is a polyether-based TPU with a reported Shore D hardness of 57, a tensile strength of 60 MPa, and an elongation break of 470%. It is also less susceptible to dynamic heat build-up with good hydroelastic stability and loses flexibility with the temperature drop. TPU-B is a polyester-based TPU with a Shore A hardness of 60, a tensile strength of ~25 MPa, and elongation at a break of 900%. It has high heat resistance, shock absorption capability, and chemical resistance and is less affected by cold temperatures. PCL (CAS-No. 24980-41-4) with a molecular number of 80,000 was in the form of pellets and purchased from Millipore Sigma. It is a biodegradable polyester with a reported low melting point of ~60 °C. Synthetic black iron oxide (Fe_3O_4>98%) nanoparticles with an average particle size of 300 nm in diameter were purchased from Alpha Chemicals. Phenylbis (2,4,6-trimethyl benzoyl) phosphine oxide (i.e., Irgacure 819 (IR819), 97% assay, CAS-No. 162881-26-7) in the form of powder and dimethylformamide (DMF) (anhydrous, $\geq$ 98%) were purchased from Millipore Sigma. All the materials were used as received.

Feedstock Processing and 3D Printing Procedures: Two feedstocks were prepared to form alternating layers within each printing line using the in-house designed and assembled 3D printer, namely, MDIW (Fig. 1 & Table 1).

Feedstock A (Fig. 1a) consists of TPU-D and PCL dissolved in DMF. First, the different weight percentages of TPU-D (i.e., 5 - 15 wt%) were added to DMF with constant mechanical stirring at 100 °C. Then, after complete dissolution of TPU-D, varying weight percentages of PCL (i.e., 5 - 20 wt%) were added to the TPU-D/DMF solution at the same temperature and stirring speed till complete dissolution. Finally, 2 wt% of IR819 was added to the TPU-D/PCL/DMF solution while cooling down to room temperature. This feedstock A was degassed via ultrasonication for 45 min before use.

Feedstock B (Fig. 1a) consists of TPU-B dissolved in DMF and Fe_3O_4 nanoparticle suspension. First, the TPU-B (i.e., 55 - 65 wt%) was added to DMF with constant mechanical stirring at 100 °C. Then, after the complete dissolution of TPU-B, the Fe_3O_4 (i.e., 7.5 wt%) was suspended in the solution using high-speed mechanical stirring and cooled down to room temperature. Finally, 2 wt% of IR819 was added to the TPU-B/Fe_3O_4/DMF solution. This feedstock B was degassed via ultrasonication before use.

Polyurethane-based polymers were chosen due to their extended- or short-chain polymer network, which is considered favorable for shape memory or fixation effects. Besides, their excellent biocompatibility can have applications in the biomedical field, such as actuators in soft robotics or regenerative tissue engineering and drug delivery devices. Similarly, PCL is biodegradable and biocompatible in the manufacturing of polyurethanes to modify its mechanical properties. Fe_3O_4 has found applications as drug carriers due to their availability and lower cost.

Three different samples were 3D-printed using the in-house MDIW platform (Fig. 1a-e), including (i) homogeneous feedstock A or B (i.e., TPU-D/DMF, TPU-B/DMF printed with three layers along the z-axis) (ii) individual mixtures (i.e., TPU-D/PCL/DMF, TPU-B/Fe_3O_4/DMF printed with three layers along the z-axis), for feedstock A & B, and (iii) multiphase layers with TPU-D/PCL/DMF as feedstock A and TPU-B/Fe_3O_4/DMF as feedstock B printed with 3–10 layers along the z-axis. All samples had similar printing procedures. For example, one MDIW

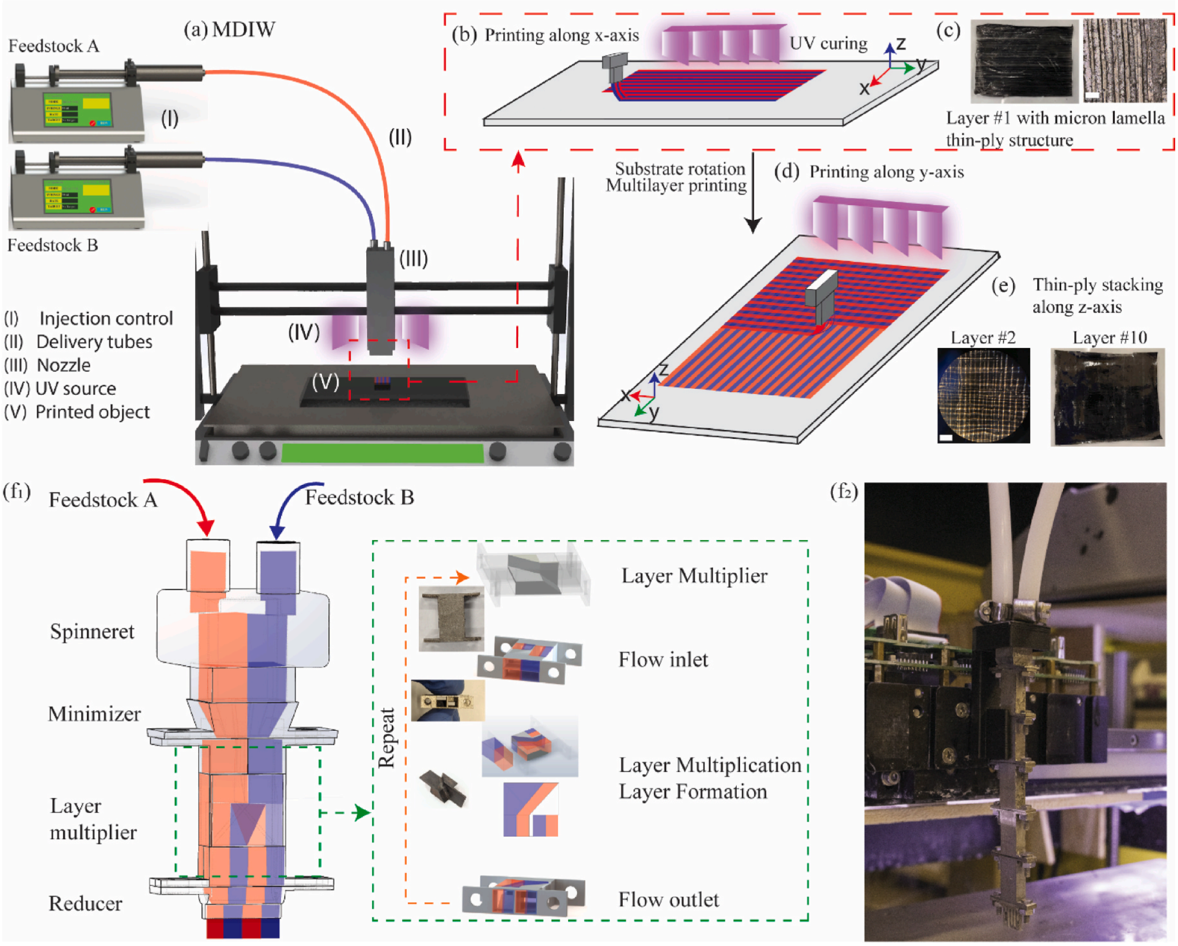

Fig. 1. The in-house developed new 3D printing, Multiphase Direct Ink Writing (MDIW), for multi-material printing with the (a) MDIW manufacturing mechanism and control systems for (b–e) in-line and out-of-plane layered structures (b) UV-assisted printing along the in-plane x-axis (i.e., comparative alignment 0°), with (c) a digital photograph of the as-printed layer #1 (i.e., one printing line contains 64 sublayers with alternating layers have feedstock A/B/A/B …) and a zoom-in optical image (scale bar of 400 μm) (d) UV assisted printing along the in-plane y-axis (i.e., comparative alignment 90°), with (e) an optical (scale bar of 500 μm) and digital photograph of the as-printed layer #2 and #10 (i.e., one printing line contains 64 sublayers with alternating layers have feedstock A/B/A/B …), (f_1) MDIW printing nozzle design contains the spinneret, minimizer, layer multipliers, and reducer, with the theoretical modeling in Fig. S2/movie S1, and (f_2) a digital photograph of the MDIW nozzle with 5 multipliers (IN718 3D printed via Concept Laser M2) mounted on the 3D printing platform with injection, deposition, and feedstock composition controls.

Table 1
Nomenclature of the test samples.

Category	Sample	Compositions				
		x/y-axis layer #	z-axis layer #	Feedstock A	Feedstock B	Rationale
3-layer, homogeneous TPU	TPU-D	64 with the sublayer domain size of ~100 μm	3	TPU-D/DMF		Control samples to examine the actuation conditions
	TPU-B			TPU-B/DMF		
3-layer polymer mixtures	TPU-D/PCL			TPU-D/PCL/DMF		
	TPU-B/Fe_3O_4			TPU-B/Fe_3O_4/DMF		
3- to 10-layer multiphase composites	3L		3	TPU-D/PCL/DMF	TPU-B/Fe_3O_4/DMF	PCL as phase switch for thermal actuation and Fe_3O_4 for magnetic actuation
	4L		4			
	5L		5			
	8L		8			
	9L		9			
	10L		10			

Note: the post-printing processing was via UV- curing for solidification purposes.

printing line along the in-plane x/y-axis contains 64 sublayers with a 100 μm domain size for each sublayer, which is consistent for all samples. The sublayers along the x/y-axis can evenly distribute the TPU-D/PCL and TPU-B/Fe_3O_4 for thermal and magnetic actuation. In addition, the excellent distribution of Fe_3O_4 can also enhance the mechanical durability of composites. An increase of the layer numbers along the z-axis varied in samples (iii) for different actuating purposes.

3-layer, homogeneous TPU: Both syringes were loaded with the same solution (i.e., (TPU-D/DMF or TPU-B/DMF)) and pumped at a constant flow rate of 1 ml/min. As a result, the homogeneous samples undergo a similar shear process to the composites (TPU-D/PCL&TPU-B/Fe_3O_4 layers) to serve as control samples.

3-layer polymer mixtures: Both the syringes were loaded with the polymer mixtures (TPU-D/PCL/DMF or TPU-B/Fe_3O_4/DMF) and pumped at a constant 1 ml/min flow rate. As a result, the TPU-D/PCL combination responds to temperature, while TPU-B/Fe_3O_4 mixtures respond to the magnetic field.

3- *to 10-layer multiphase composites:* Feedstock A consisted of TPU-D/PCL/DMF loaded in one syringe, and feedstock B consisted of TPU-B/Fe_3O_4/DMF loaded in the other syringe (Fig. 1a), pumped at a 1 ml/min flow rate. The layers along the out-of-plane z-axis varied from 3 to 10 layers (Fig. 1b-e).

Characterizations: The rheology studies were conducted at room temperature (RT) using a cone-and-plate rheometer (Discover Hybrid Rheometer HR2, TA Instruments). The samples were dropped on a 40 mm, 2° Peltier steel cone plate with the viscosity measurement at an increasing strain rate of 0.001–8000/s, a truncation gap of 100 μm, and a trim gap of 50 μm. Any excess flow of the sample was cleaned before the test to prevent edge fracture for accurate results. The tensile tests at room temperature and dynamic mechanical analysis (DMA) with the environmental control chamber were conducted using the rectangular tensile setup (Discover Hybrid Rheometer HR2, TA Instruments). A gauge length of 10 mm was set constant for both tests. The tensile tests were conducted on all samples till the maximum limit of the machine to find the elastic properties or till a fracture occurred (Fig. 2).

The shape memory effect (SME) was tested via the cyclic thermo-mechanical procedures using the DMA (Fig. 3a_1-a_5). The test was conducted at two different tension strains (i.e., 250% and 125%), both above the samples' yield point and potentially causing plastic deformation (Fig. 3a). First, the samples with a 10 mm x 5 mm x 0.18 mm dimension were clamped between the jaws (Fig. 3a_1) and stretched uniaxially at a constant strain rate of 300 μm/s up to 25 mm (i.e., 250% strain) and 12.5 mm (i.e., 125% strain), respectively (Fig. 3a_2). After stretching, the samples were frozen at −20 °C using liquid nitrogen for 15–20 min to fix the shape inside the environmental chamber (Fig. 3a_3). Afterward, the bottom jaw of the testing setup was unclamped, and the sample was heated to 60 °C in the environmental chamber, with the shape recovery process completed within 2–3 min (Fig. 3a_4-a_5). During each test cycle, the initial length and every subsequent length change in each stretching-freezing-heating-recovering cycle were measured using an in-built digital measuring system of the machine to calculate shape recovery. This process was continuous for a maximum of 15 cycles (until a fracture failure) for each sample to evaluate responsivity and reusability to demonstrate stimuli-responsiveness and shape recovery efficiency.

A differential scanning calorimetry (DSC) (Discovery DSC 250, TA Instruments) was performed in three cycles (i) heating from −80 °C to 250 °C; (ii) cooling from 250 °C to −80 °C, and (iii) heating from −80 °C to 250 °C at a constant rate of 10 °C/min in a nitrogen atmosphere. In addition, thermogravimetric analysis (TGA) (Discovery TGA 550, TA Instruments) was conducted for dry and wet samples (water-soaked) to understand the thermal transitions in the air and liquid media. The TGA was performed from RT to 900 °C at a heating rate of 10 °C/min in an inert atmosphere using nitrogen.

3. Results and discussions

3.1. Design of MDIW and the 3D printing uniqueness

The MDIW 3D printing has not been reported in any literature except ours (e.g., the Stage-I platform [42]). Thus, a brief description of its unique design will be presented here. Fig. 1a illustrates the setup of the MDIW. This 3D printing platform contains (i) injection controls for material feedstocks, (ii) programming/machine controls for printing path and structural design, (iii) delivery tubes, (iv) printhead for printing ink deposition with the UV system, and (v) printed objects. During the 3D printing for composite layers, feedstock A (i.e., TPU-D/PCL/DMF) and feedstock B (i.e., TPU-B/Fe_3O_4/DMF) (see chemical compositions in Table 1) got injected from two syringes, respectively. These two syringes were connected to the same printhead to form in-plane layers along either x- or y-axis (Fig. 1b–e). Thin in-plane layers could distribute different materials at selective locations as desired that may otherwise compromise the printed microstructures or properties. For example, non-compatible materials may form polymer phase separations or particle agglomerations that cause crack propagation and mechanical failures [14,43–45]. As a result, the uniform

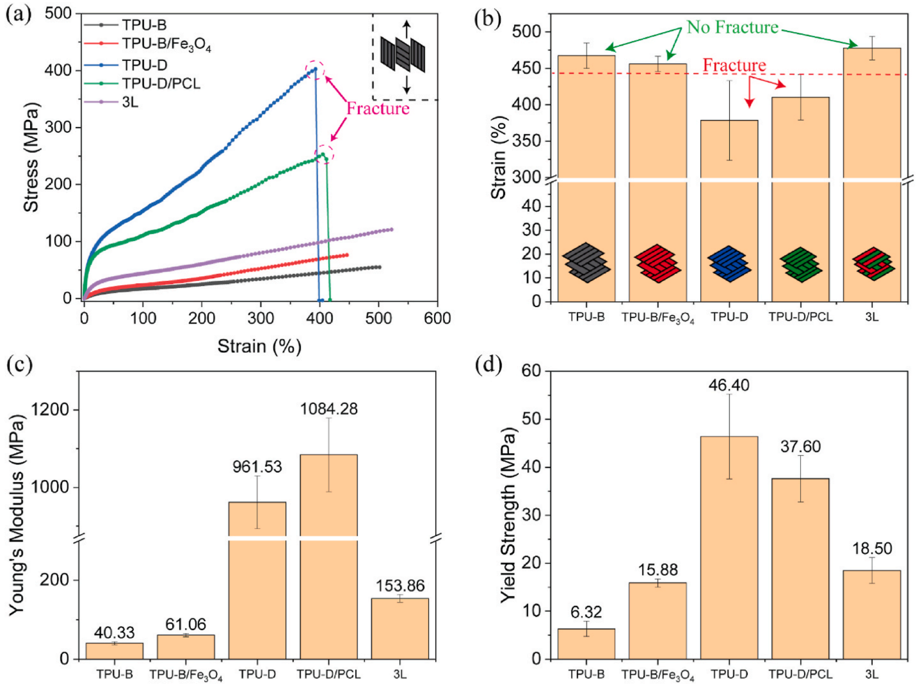

Fig. 2. Tensile test properties of the homogeneous polymers (i.e., TPU-B, TPU-D) and mixtures (i.e., TPU-B/Fe_3O_4, TPU-D/PCL) with three printed layers along the z-axis, and multiphase composites (3L) with each z-axis layer containing x/y orthogonal textures of $0^o/90^o/0^o$ and compositions of TPU-B/Fe_3O_4 and TPU-D/PCL in alternating x/y layers, (Fig. 1b), (a) stress-strain curves, (b) max strain up to ~475% to examine stretchability/fracture points, (c) Young's modulus, and (d) yield strength of as-printed samples.

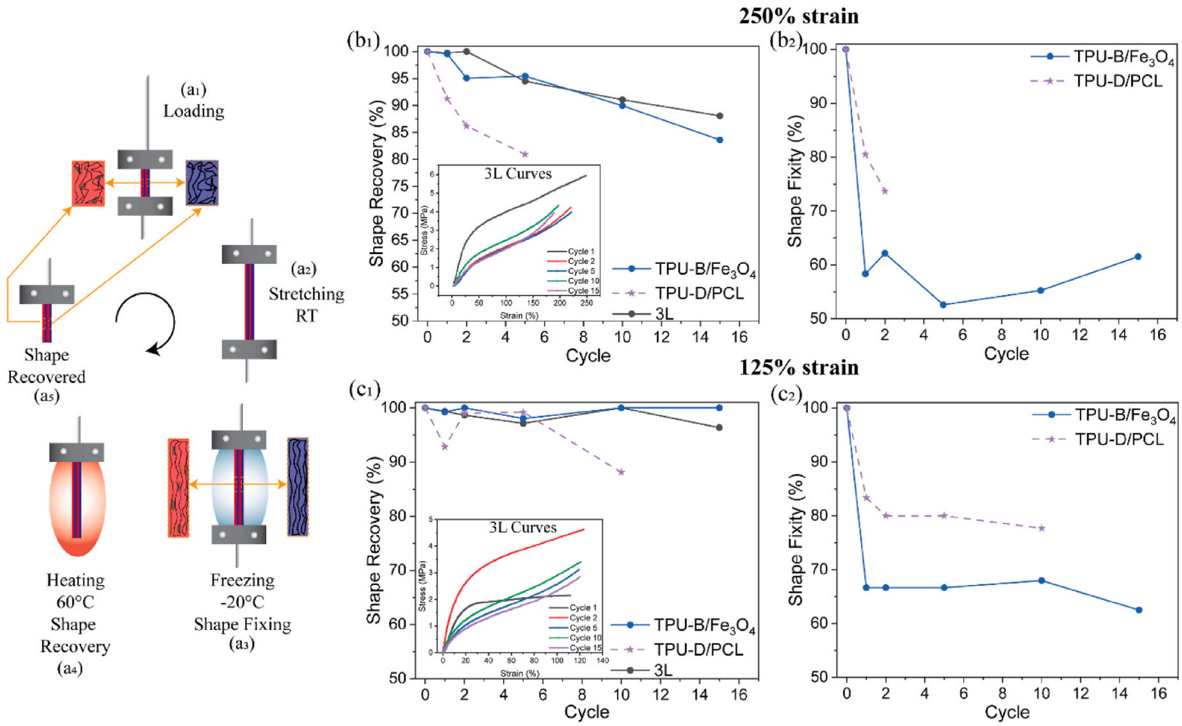

Fig. 3. Programmed cyclic loading and unloading tests via the dynamic mechanical analysis (DMA) to study the shape memory effect (SME) of the layered, multiphase composites with (a_1-a_5) illustrations of the thermo-mechanical SME test using a DMA; shape recovery of various samples (i.e., TPU-B/Fe_3O_4, TPU-D/PCL, 3L, as shown in Fig. 2) up to 15 cycles under a strain of (b_1) 250%, showing deteriorated recovery degree, and (c_1) 125%, showing efficient recovery for 3D printed, layered composites (i.e., 3L), with the insert figures of the fatigue tests at room temperature at a cycle of 1, 2, 5, 10 and 15 and their shape fixity under a strain of (b_2) 250% (TPU-D/PCL fractured beyond cycle 5) and (c_2) 125%.

nanoparticle distribution (e.g., Fe_3O_4) would enhance the composite's mechanical, magnetic, and thermal properties. More importantly, the one-step alternating deposition of layers from one nozzle (i.e., the multi-channel printhead used here instead of a single-channel printhead/needle in most multi-material 3D printing) would avoid phase mismatches, interfacial debonding, and pore generations in general extrusion-based 3D printing (e.g., FDM). Apart from the materials used as examples in this study, more combination of materials is possible to provide different stimuli responsiveness. Other material combinations (polymer and nanoparticle) including TPUs and non-polyurethane polymers as examples from the literature are given in Tables S1 and S2.

The printhead design (Fig. 1f) is critical to the in-plane microlayer formability. Fig. 1f illustrates the components of the MDIW printhead, consisting of (i) spinneret, (ii) minimizer, (iii) layer multiplier, and (iv) reducer. A layer multiplier is essential in dividing feedstock A and B before rearranging them from two to four layers (Fig. 1f_1). A number of n multipliers connected consecutively will generate 2^{n+1} layers within each printing line. Therefore, our use of 5 multipliers generated 64 sublayers within a 10 mm-wide printing line, leading to an in-line domain size of ~100 μm (Fig. 1c). Higher than 64 layers were not possible due to higher interlayer dispersion of Fe_3O_4 nanoparticles and prevented uniform layers formation (Fig. S1). The photographic inset in Fig. 1f_1 shows the surface and internal structures of the layer multiplier and movie S1 shows a flow simulation in the nozzle. Another parameter important for successful layer formation is the rheology matching between feedstock A/B to avoid layer disruptions. Fig. S2 of the fluid flow simulation shows the layer formability between fluids with similar viscosity, while different flow behaviors lead to layer disruptions (Fig. S3). Improving this printing resolution from the microscale to the nanoscale is feasible simply with a higher number of multipliers, while this research only focuses on multiplying mechanisms to show the actuation capabilities in unique layers.

The printed layers on glass substrates solidified immediately after deposition with *in-situ* curing (i.e., via a 60 W, 405 nm UV source attached below the axil of the printhead, Fig. 1b). Fig. S4 shows the FTIR analysis of TPUs with and without photoinitiators displaying new bond formation due to cross-linking when exposed to UV light. The layers along the out-of-plane z-axis (i.e., layers in the layup) were oriented at 0°/90° orthogonal for producing isotropic properties, as shown in Fig. 1d. For example, Fig. 1b–c illustrate the printing of one thin ply structure (1L) with an orientation of 0°. Fig. 1d represents the printing of the second layer (2L) with a direction of 90°, and Fig. 1e shows the 0°/90° stacking with 2 layers (2L) up to 10 layers (10L). Fig. S5 shows the cross-sectional optical images of the multiphase samples (i.e., 3L, 5L, and 10L). More importantly, the as-printed multiphase composites were quickly printable (e.g., areas as large as 21 × 21 cm sheet-sized composites containing up to 10 layers along the z-axis were complete within 40 min using 70 ml of each feedstock), showing the faster, larger-area printability via our MDIW than most current bio-plotting methods [42]. Fig. 1f_2 is a digital photograph of the printhead nozzle mounted on the MDIW platform.

3.2. Mechanical characterizations

The mechanical properties were obtained through tensile tests to determine the structural integration during actuation conditions. These tested samples include the TPU-B, TPU-B/Fe_3O_4, TPU-D, TPU-D/PCL, and multiphase composite layers of TPU-B/Fe_3O_4- TPU-D/PCL as an example (Fig. 2a-b), see chemical compositions and material rationals in Table 1). Among them, the TPU-D and TPU-D/PCL fractured with a failure strain of 395% and 440%, respectively, while the rest of the samples were intact at a strain of 475%, showing the elastomer's mechanical robustness with large stretchability (Fig. 2b). The addition of PCL acts as a functional chain extender to form a crystallized hard segment within the amorphous soft segment of TPU-D. This soft-hard segment mixture would improve shape fixation with the low melting point (~60 °C) in PCL to initiate shape recovery and increase stimuli-responsiveness [46,47]. A comparison between TPU-B and TPU-B/Fe_3O_4 (Fig. 2c and d) showed the effective reinforcement of Fe_3O_4 in enhancing elastic modulus and strength (i.e., determined by the 0.2% strain offset method since there is no yield point due to the dominant TPU content). These enhanced mechanical properties also suggested good dispersion quality of the iron oxide particles, which would benefit the selective particle locations in layers and enable magnetic responsiveness. The multiphase composites (3L) contained TPU-B/Fe_3O_4 and TPU-D/PCL as alternating sublayers within each printed line along the in-plane x/y-axis and 3 layers along the out-of-plane z-axis (0°/90°/0° orientations among z-axis layers, as shown in Fig. 2b insert schematics). Also, the 3L composites exhibited large deformations (>475%) to ensure structural integrity during actuation and intermediate modulus and strength (Fig. 2b-d) consistent with composite mechanics.

3.3. Shape memory effect (SME) analysis

All samples subjected to a cyclic thermo-mechanical analysis were under temperature and force control (Fig. 3a_1-a_5) to show their shape memory effects. The hybrid TPU-D/PCL regions are capable of shape fixing and shape recovery, with the PCL consisting of stiff crystals responsible for shape fixing and temporary shape retention upon stretching (Fig. 3a_2-3a_3), while the TPU-D of amorphous molecules recovering to the original dimensions by releasing the deformation energy upon heating (Fig. 3a_4-3a_5). Applying the uniaxial stress would orient the polymer chains and enable the segmental movement of the molecules with a build-up of elastic strain energy [48–50]. To prevent the polymer chain from immediate recovery and stabilize the movement of the molecules, freezing the sample below the transition temperature would help fix the shape (Fig. 3a_2-3a_3). When exposed to a temperature near or higher than the transition temperature, the oriented polymer chain shift from the glassy to rubbery state, relaxing the molecules to a more thermodynamically stable form (Fig. 3a_4-3a_5). This strain energy release leads to the polymer chains' relaxation and subsequent shape recovery.

This cyclic thermo-mechanical test used extremely high-tension strains (i.e., 250% in Figs. 3b and 125% in Fig. 3c) to examine the shape recovering capability. After each thermo-mechanical cycle, the shape fixity and recovery for *N* cycles can be calculated as follows [9,51,52],

$$\text{Shape fixity}, R_f = \frac{\varepsilon_u(N)}{\varepsilon_m(N)} \qquad \text{Equation 1}$$

$$\text{Shape recovery}, R_r = \frac{\varepsilon_u(N) - \varepsilon_p(N)}{\varepsilon_u(N) - \varepsilon_p(N-1)} \qquad \text{Equation 2}$$

Where *N* is the number of cycles, ε_u is the strain after unloading (Fig. 3a_3), ε_m is the strain at maximum load, and ε_p is the final recovered strain (Fig. 3a_5). At a strain of 250% (Fig. 3b), the degree of shape recovery decreased with cycles for all samples. In addition, the TPU-D/PCL deteriorated the most rapidly (i.e., 80% recovery after only 5 cycles though the shape fixing ratio stabilized 75%–80%) due to its rigidness. As compared, the TPU-B/Fe_3O_4 and 3L composites displayed ~85% and 90% recovery, respectively, even after 15 cycles. For the aim of better recovery capability and actuation responsiveness, the tension strain during the thermo-mechanical analysis was reduced (i.e., 125% in Fig. 3c). For example, the TPU-D/PCL retained the original dimensions before fracturing at a cycle number of 10. The TPU-B/Fe_3O_4 and 3L composites displayed a recovery beyond 95% up to a cycle of 15 because of their highly rubbery state. As a result, TPU-B/Fe_3O_4 showed better recovery but worse shape fixing capability than the TPU-D/PCL (Fig. 3b-c), justifying the combination of both compositions in the 3L composites for highly efficient actuating behaviors. Besides, the cyclic fatigue tests for 3L composites at room temperature (insert stress-strain curves in Fig. 3b-c) also showed higher elasticity under lower tension strains.

3.4. Thermal analysis

Thermal transitions, such as glass transition (T_g), recrystallization point (T_c), and melting temperature (T_m), are essential parameters to explore shape memory effects and thermal actuation conditions [23,53]. Fig. 4a shows the DSC curves during the heating-cooling-heating cycles. Among these samples, PCL pellets showed a T_m~59 °C and T_c ~31 °C during the 1st heating and cooling procedures, respectively, while this melting temperature dropped to T_m~57 °C during the 2nd heating. This melting point drop was due to the molecular reorganization during the 1st melting. In comparison, the TPU-D displayed a T_m ~170 °C, a much higher melting transition than PCL that could degrade PCL molecules (Fig. 4a_1). This degradation explained the PCL's melting peak appearing in TPU-D/PCL (Fig. 4a_1) and its disappearance in the cooling/reheating cycles (Fig. 4a_2-4a_3). Moreover, the TPU-B showed a $T_g \sim -50$ °C but did not show a melting T_m, suggesting its amorphous feature (Fig. 4a_1-4a_3) was necessary for thermal stimuli responsiveness.

Considering the shape fixing of TPU-D/PCL due to their crystalline compositions and the shape recoverability of TPU-B/Fe_3O_4, the z-axis layer effects on the actuation feasibility and efficiency were under investigation. Fig. 4b_1– 4b_3 showed the transitions of composites with different layers (i.e., 3L, 4L, 5L, 8L, 9L, 10L). Though with a small amount, the melting peaks of PCL remained within a range of 40–50 °C for the 1st heating cycle (Fig. 4b_1 & 4c). The PCL recrystallization during the cooling temperature varied from 60 to 80 °C (Fig. 4b_2 & 4c), implying the confinement of channels within each x/y layer that enhanced the crystallization upon cooling. However, the reheating did not show the PCL melting, possibly due to the degradation with the high heating up to 250 °C (Fig. 4b_3), which was also consistent with TPU-D/PCL thermal curves (Fig. 4a_1-4a_3). TPU-B's glass transition of T_g ~ −50 °C was consistent during the heating-cooling-reheating cycles, suggesting its thermal stability guaranteeing subsequent actuation behaviors without fatigue. Therefore, the actuation condition would be ideal in the vicinity of PCL melting peaks (40–65 °C) to avoid PCL degradation and retain TPU glass transition or melting.

To understand the moisture/liquid influences, Fig. 4d represents the TGA curves of the multiphase composite samples (i.e., 3L, 4L, 5L, 8L, 9L, 10L) in dry and wet conditions. In dry condition, the 10% weight loss of the multiphase composites were ~250 °C, which was also the upper limit temperature for the DSC cycle. The samples were soaked in water for 1 h in wet conditions before performing the TGA test to validate the responsiveness in wet conditions. As a result, there was a quick weight loss due to evaporation of absorbed water, and at a higher temperature (>350 °C), the weight loss stabilization was similar to the dry samples. This water loss indicated the material compositions in dry and wet environments, influencing their mechanical stiffness, thermal transition kinetics, and stimuli responsiveness to be examined in actuation experiments.

3.5. Thermal actuation via response time-temperature-layer number relationship studies

All rolled structures with the same dimensions went through the stimuli-responsiveness experiments to establish the relationship between expansion time(s)-actuation temperature (°C)-thickness/layer number (i.e., 3L–10L) (Fig. 5). These samples were 5 × 5 cm in a square, rolled by freezing the samples at −20 °C for 15–20 min. The rolling direction was along the diagonal axis (45°) (Fig. 5a-b) or the x/y-axis (90°) (Fig. 5c-d). The expansion time(s) started from the deposition of rolls in different media (i.e., the air in Fig. 5a/5c and the water in Fig. 5b/5d) and ended with the state of complete unrolling. All layered composites had fully unrolled recovery via the stimuli temperature of 40–65 °C in air and water (Fig. 5). This efficient responsiveness upon heating was consistent with the thermo-mechanical analysis (Fig. 3) and thermal transition experiments (Fig. 4), though the rolling strain subjected was much smaller than the SME analyses (<10% in rolling vs.

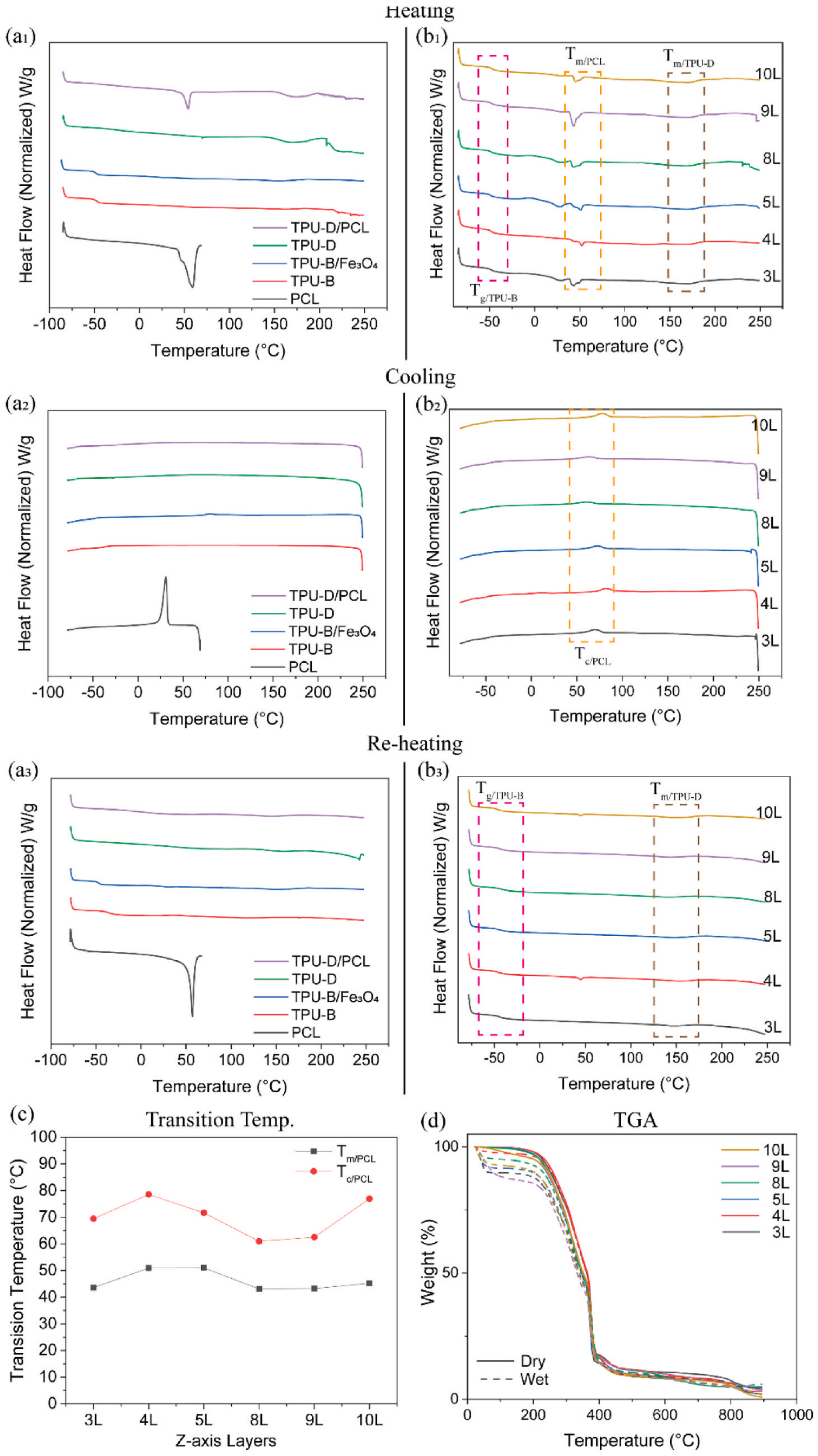

Fig. 4. DSC heating-cooling-reheating cycles showing glass (T_g), melting (T_m), and crystallization (T_c) temperatures for (a_1-a_3) homogeneous and polymer mixture samples (i.e., 3 layer TPU-D/PCL, TPU-D, TPU-B/Fe_3O_4, TPU-B, and PCL) and (b_1-b_3) multiphase composites (i.e., 3L, 4L, 5L, 8L, 9L, 10L); (c) transition temperatures as a function of layers in the multiphase composites from (b); and (d) TGA thermal stability of dry and wet (water-soaked) composites.

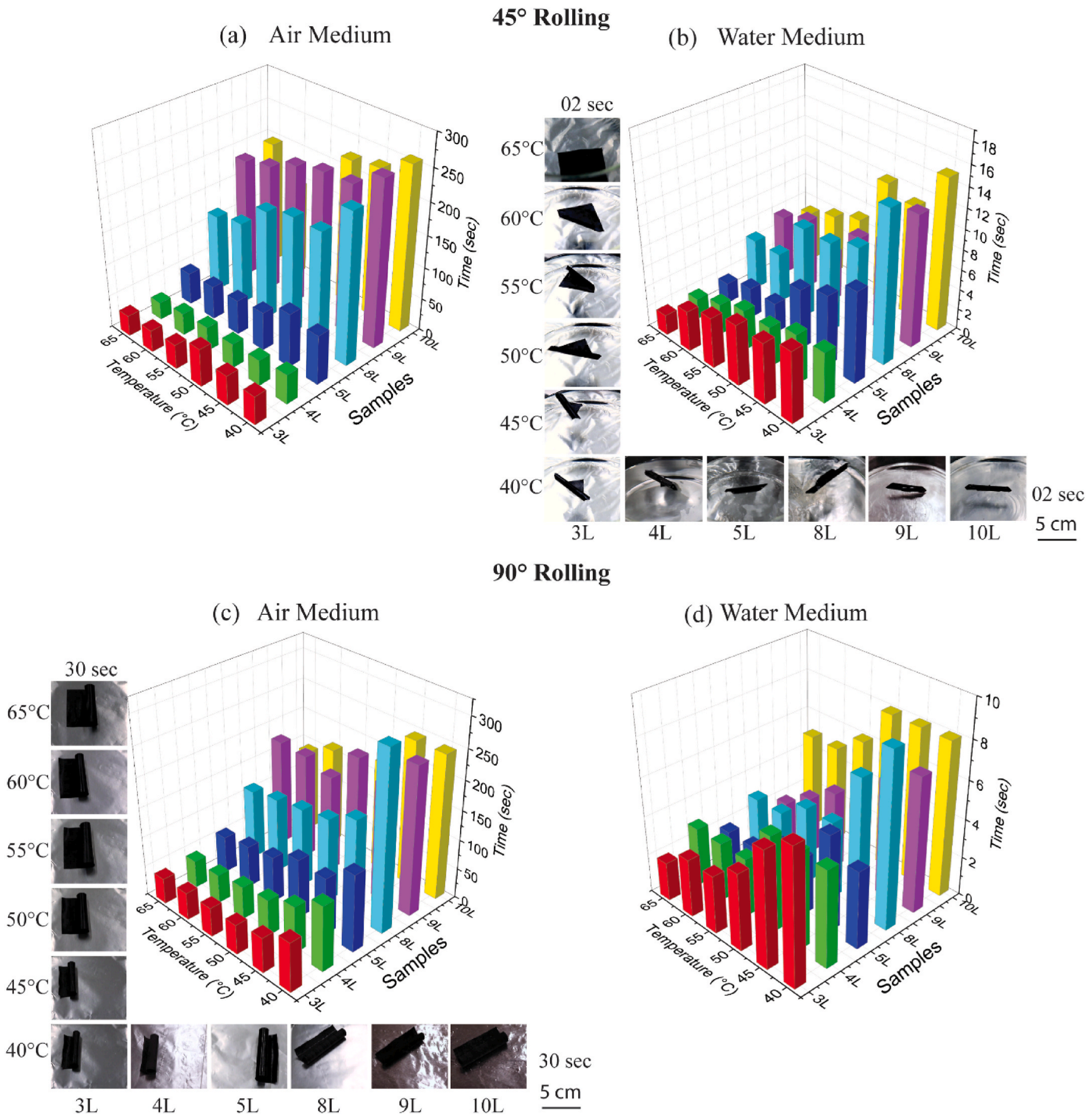

Fig. 5. Stimuli-responsiveness for layered composites during thermal actuation at different conditions, with the full expansion of 45°-rolled layers in the medium of (a) air and (b) water, full expansion of 90°-rolled layers in the medium of (c) air and (d) water for establishing the expansion time (s)-actuation temperature (°C)-composite layers (i.e., 3L–10L) relationships.

125% and 150% in DMA tests, Fig. 3). Specifically, the TPU-D/PCL was highly efficient in shape fixing (active phase) (Fig. S6a), with PCL acting as the switching element for initiating the actuation upon heating. At the same time, TPU-B/Fe_3O_4 had a high shape retention effect (passive phase) (Fig. S6b). The maximum rolled strain impacted on the multiphase composites was calculated theoretically (Equation (3)) and varied from 3% to 10%, respectively, with the increasing thickness (3L–10L), which was much less than the strain used for the SME analysis (125% and 150%, Fig. 3). The shape was highly transitional between a fixed state in rolls upon cooling and an actuation state upon heating in either air or water.

The actuation time increased consistently with the temperature decrease or layer number/sample thickness increase, both of which affect the bending strain/stress according to the bending theory (Equation (3)&(4)) [54,55]. For example, 3L composites rolled at 45° had an expansion time of 45s and 72s in the air at a temperature of 65 °C and 40 °C, respectively (Fig. 5a). As a comparison, a larger layer number significantly improved the resistance to similar thermal stress generated in thinner layered structures, showing a response time of ~140s, ~235s, and ~260s for 4L, 8L, and 10L composites, respectively (Fig. 5a).

$$\varepsilon_r = h/2r \quad \text{Equation 3}$$

$$\sigma_r = My/h^3 \quad \text{Equation 4}$$

where *h* is the thickness, *r* is the rolled inner radius, *M* is the moment of inertia, and *y* is the bending modulus.

Similarly, the response time consistently increased with the temperature decrease and layer increase when the actuation media changed from air to water (Fig. 5b). According to the TGA analysis, the water was present in composites after soaking and softening the layers with lower bending modulus and decreased resistance to thermal stress. Therefore, the unrolling time decreased much more than in air; for example, the same 3L showed an expansion time of 2s and 17s in the water at the temperature of 65 °C and 40 °C, respectively (Fig. 5b). The faster response within the water bath environment was also due to more efficient heat transfer between the actuation objects and water than with air (e.g., the rolled structures had lower temperature distribution further away from the hot plate-layer contact surfaces while the heat convection is more uniform for soaked layers in water). The digital images in water environments also demonstrated the rolled structures at a time of 2s and their different expansion states upon heating to elevated temperatures (i.e., 40–65 °C) and different layer numbers at a specific temperature (i.e., 40 °C at 2s) (photos in Fig. 5b).

The rolling direction is another critical parameter to control the layer's stimuli-responsiveness. Fig. 5c-d represent the time study in air and water media for samples rolled at 90° vs 45° in Fig. 5a-b. Similar to 45°-rolled layers, the actuation with 90°-rolled composites also showed (i) longer response time with decreased temperatures and increased layer numbers in air and water, respectively, and (ii) much faster responsiveness in water than air for samples of specific layer number and a programmed temperature. The digital images in the air medium also demonstrated the rolled structures at a time of 30s and their different expansion states upon heating to elevated temperatures (i.e., 40–65 °C) and different layer numbers at a specific temperature (i.e., 40 °C captured at 30s) (photos in Fig. 5c).

Shape-morphing microrobots have broad applications, including drug delivery in the human body for cancer cell treatment, oil leakage collection, or sewage water treatment [56–60]. The unrolling procedures for 5-layered (5L) composites also demonstrated the consistency in stimuli-responsiveness as a function of time for different rolling directions in the air (Fig. 6). The complete expansion of the 45°-rolled and 90°-rolled layers took 76s and 58s, respectively (Fig. 6a_1 & **6a_2**), to expose and deliver drugs (dotted circle) at 60 °C, with the delivery time programmable via temperatures, composite layers, and environmental media (Fig. 5). The hotplate-sample thermal conduction was measured immediately after the complete expansion using a thermal imaging camera in the 45°-rolled (Fig. 6b_1–6g_1) and 90°-rolled (Fig. 6b_2–**6g_2**) composites. The sample temperatures were consistently lower than the heating source for both conditions, e.g., 35.6 °C and 35.7 °C for 45°-rolled (Fig. 6b_1) and 90°-rolled (Fig. 6b_2) composites, respectively, when the hotplate temperature was 40 °C. This efficient heat conduction for rolled shells is also useful for expandable objects in space missions (e.g., antenna, rocket shields, solar panels) [61–63].

3.6. *Complex shape actuation demonstration*

Understanding the thermal actuation mechanism and the effects of temperature and sample layers also facilitated the design of more complex structures for stimuli-responsiveness purposes. These complex shapes included multifold, cylindrical, and helical (digital images in Fig. 7). Similar to the previous samples of square sizes, these complex shapes got frozen at −20 °C for shape fixing for 15–20 min before stabilizing (Fig. 7a_1-a_3). Following this, the samples went through the actuation procedure with a programmed temperature of 60 °C on a hot plate (air medium). The responsiveness depended upon the dimensions and structural complexities. For example, the multifold origami structure (5 × 5 cm), with one major fold along the center and two minor folds perpendicular to the primary fold line, expanded from an accordion-like stacking (Fig. 7b_1) to half-unfolded (Fig. 7c_1) and fully expanded (Fig. 7d_1) within 4 min. The creases from the folding were

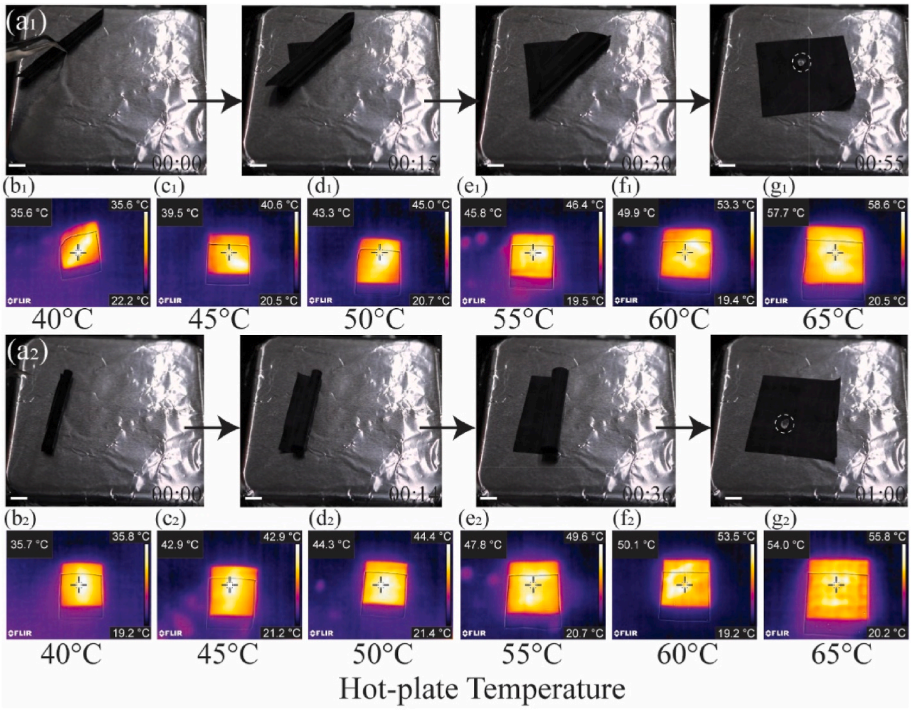

Fig. 6. Digital photographs of thermal actuation for 5-layered (5L), (a_1) 45°-rolled, and (a_2) 90°-rolled composites showing varying expansion degrees as a function of time on a hot plate of 60 °C, with thermal images showing heat transfer and temperature distributions across the completely expanded layers for (b_1-g_1) 45°-rolled and (b_2-g_2) 90°- rolled composites at different hotplate temperature (40–65 °C with a step-wise temperature increase of 5 °C) (scale bar of 1 cm).

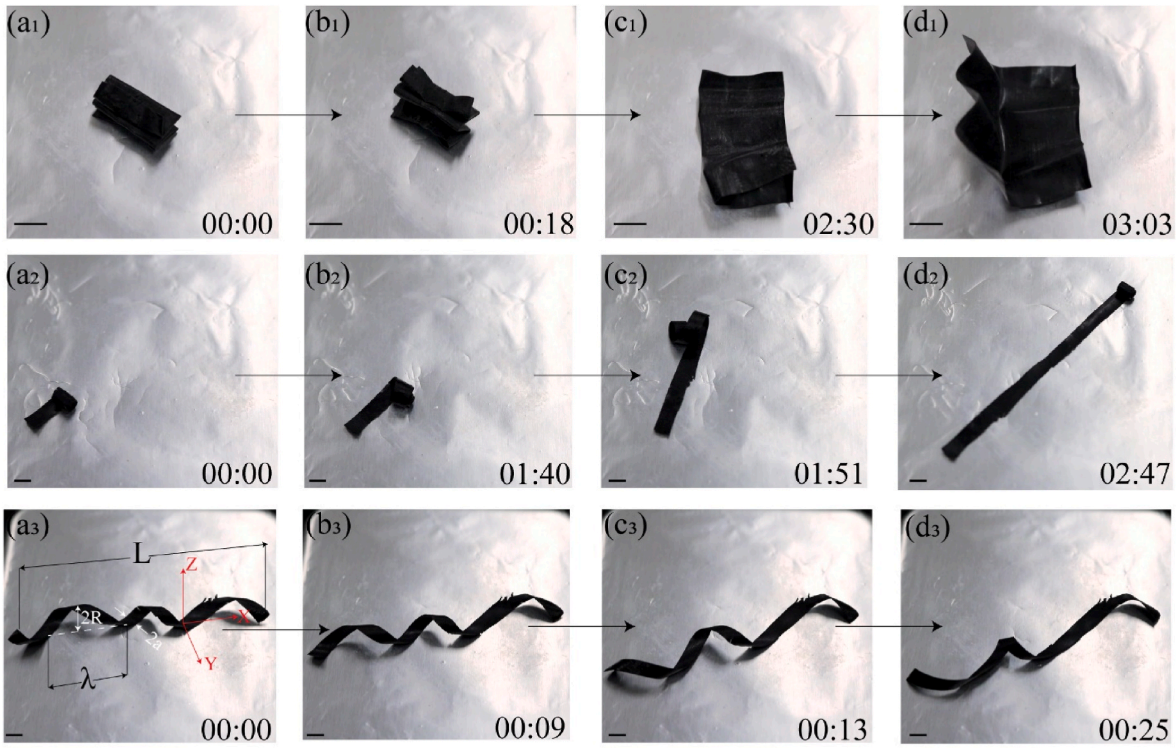

Fig. 7. Thermal actuation for complex shapes of (a_1-d_1) multifold origami, (a_2-d_2) cylindrical rolls, and (a_3-d_3) helix wrinkles [R: cross-section radius, λ: wavelength, a: radius along z-axis] (scale bar of 1 cm).

present after completion, but the sample was still in good condition for multiple fixation-recovery uses. Fig. 7a_2-7d_2 are the unrolling images of thin tape cylinders 21 cm long with a rolled inner diameter of 2.5 mm. The shape fixing procedure took ~45 min at a temperature of −20 °C due to the large number of rolls (Fig. 7a_2). As a comparison, the actuation on a hotplate at 60 °C took ~1 min for the sample to start expansion and ~3 min to unroll fully.

Fig. 7a_3-7d_3 are the actuation digital images of a helix structure (i.e., the original length of $L_o = 5$ cm, wavelength $\lambda_o = 2$ cm, and cross-section projection on the y-z plane has a radius $2a = 5$ mm for the projected circle). The helix showed a time-dependent space curve with the mathematical equations given for the 3D helix as below [64–66],

$$x\,(t,u) = ht + \frac{Ra\,\sin\,u}{\sqrt{R^2 + h^2}} \qquad \text{Equation 5}$$

$$y\,(t,u) = Rcos(t) - a\,\cos\left(t\right)\,\cos\left(u\right) + \frac{ha\,\sin\,(t)\,\sin\,(u)}{\sqrt{R^2 + h^2}} \qquad \text{Equation 6}$$

$$z\,(t,u) = Rsin(t) - a\,\sin\left(t\right)\,\cos\left(u\right) - \frac{ha\,\cos\,(t)\,\cos\,(u)}{\sqrt{R^2 + h^2}} \qquad \text{Equation 7}$$

where t is the number of loops, $u \sim [0, 2\pi]$, h is a mathematical constant, R is the radius of the helix, a is the cross-sectional dimension of the helix, and 2πh is the pitch length. An actuation was at 60 °C in the air as evidenced by the change in the outer radius (R) and the pitch length (π) (Fig. 7a_3-7d_3). The actuation of the structure was faster than the multifold or rolled cylinders due to smaller strains. Fig. 7d_3 represents an actuation time of 25s, with a much longer wavelength but not a fully actuated shape due to the lack of efficient contact along with the helix directions.

3.7. *Magnetic responsiveness*

Iron oxide magnetic nanoparticles have good magnetic stability, moderate operating temperature, high corrosion resistance, and are relatively inexpensive. In addition, the uniform distribution of Fe_3O_4 nanoparticles can enhance mechanical durability (Fig. 2c-d), and as a ferrimagnetic material, would induce magnetic responsiveness (Fig. 8 a_1) [67,68]. As a demonstration of magnetic interactions, a 10L multiphase composite sample was used for fixed-end rotations in the air (Fig. 8a_2) and unrestricted movement on flat surfaces (Fig. 8a_3). With a small amount of iron oxide loading (7.5 wt%), the layered composites showed highly efficient attractions to the magnet and quick movability, as shown in Fig. 8b-d. Fig. 8b_1-b_4 represent the fixed end rotation of hinge movement of the sample at ~1 cm/s. At the same time, Fig. 8c_1-c_4 represent non-uniform flipping, and Fig. 8d_1-d_4 of the controlled rolling of the samples following the magnetic field direction. With pre-magnetized attraction and repulsion effects, the iron oxide magnetic nanoparticles in shape-morphing objects can have broad applications, e.g., as a constant agent in magnetic resonance imaging (MRI), targeted drug delivery vehicles, and chemotherapy that will be our future research focus [69–71].

4. Conclusion

The newly introduced MDIW 3D printing mechanism successfully combined the (1) polyether-based TPU-D with PCL and (ii) polyester-based TPU-B with Fe_3O_4 particles as feedstocks. Each printing line consisted of 64-layers with each layer domain size of ~100 μm containing different feedstock, generating synergy between mechanical robustness and actuation functions. The SME analysis proved the load-bearing capability with high strains up to 250% and demonstrated the shape fixing due to TPU-D/PCL and shape recoverability due to TPU-B/Fe_3O_4. The DSC and TGA thermal analysis predicted the transition temperatures and thermal stability in different media necessary for programming the shape memory actuation. The varying layer numbers/thickness (i.e., 3L, 4L, 5L, 8L, 9L, and 10L), modified temperatures (i.e., 40–65 °C), and different media (i.e., air and water) influenced the composite responsiveness. The established time-temperature-dimension relationship and magnetism-responsiveness allowed programmable

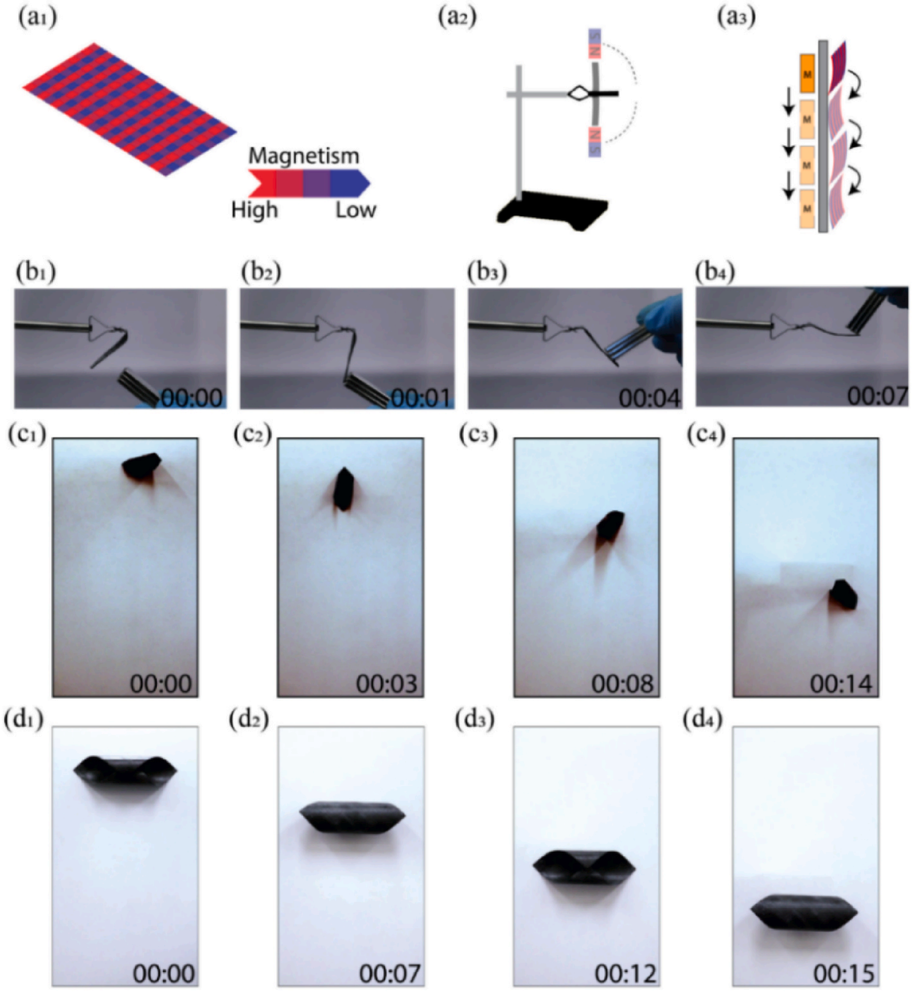

Fig. 8. Demonstration of magnetic stimuli-responsiveness of the as printed composites (10L) with the (a_1) illustration of the magnetic field-iron oxide nanoparticle interactions via (a_2) fixed-end rotations in the air and (a_3) free movement on flat surfaces, with digital images of this magnetic responsiveness of (b_1-b_4) fixed-end rotations and (c_1-c_4) free movement of flipping and (d_1-d_4) free movement of rotations.

actuators (e.g., multifold accordion-like structures or helix), suggesting broad applications in intelligent devices, targeted drug delivery, space transportation, and energy storage.

Author statement

Dharneedar Ravichandran: Conceptualization, Methodology, Sftoware, Validation. Formal analysis, Investigation, Writing – original draft, Writing – Editing, Visualization. Mounika Kakarla: Software, Methodology, Validation, Data curation, Writing – Review. Weiheng Xu: Software, Validation, Writing – Review. Sayli Jambulkar: Software, Validation, Writing – Review. Yuxiang Zhu: Software, Validation, Writing – Review. Mohammed Bawareth: Writing – Review. Nathan Fonseca: Writing – Review. Dhanush Patil: Writing – Review. Kenan Song: Conceptualization, Validation, Resources, Writing – review & editing, Supervision, Project administration, Funding acquisition

Declaration of competing interest

The authors declare that they have no known competing financial interests or personal relationships that could have appeared to influence the work reported in this paper.

Data availability

Data will be made available on request.

Acknowledgment

We thank NSF for the CAREER award (# 2145895) and FACE Foundation for the TJF grant. We also thank BASF for providing the raw materials.

Appendix A. Supplementary data

Supplementary data to this article can be found online at https://doi.org/10.1016/j.compositesb.2022.110352.

References

[1] Podstawczyk D, Niziol M, Szymczyk-Ziółkowska P, Fiedot-Tobola M. Development of thermoinks for 4D direct printing of temperature-induced self-rolling hydrogel actuators. Adv Funct Mater 2021;31:2009664.
[2] Weng S, Kuang X, Zhang Q, Hamel CM, Roach DJ, Hu N, et al. 4D printing of glass fiber-regulated shape shifting structures with high stiffness. ACS Appl Mater Interfaces 2021;13:12797–804.
[3] Hwang G, Paula AJ, Hunter EE, Liu Y, Babeer A, Karabucak B, et al. Catalytic antimicrobial robots for biofilm eradication. Sci Robot 2019;4:eaaw2388.
[4] Lu H, Yao Y, Huang WM, Leng J, Hui D. Significantly improving infrared light-induced shape recovery behavior of shape memory polymeric nanocomposite via a

synergistic effect of carbon nanotube and boron nitride. Compos B Eng 2014;62:256–61.

[5] Xu X, Fan P, Ren J, Cheng Y, Ren J, Zhao J, et al. Self-healing thermoplastic polyurethane (TPU)/polycaprolactone (PCL)/multi-wall carbon nanotubes (MWCNTs) blend as shape-memory composites. Compos Sci Technol 2018;168:255–62.

[6] Xia Y, He Y, Zhang F, Liu Y, Leng J. A review of shape memory polymers and composites: mechanisms, materials, and applications. Adv Mater 2021;33:2000713.

[7] Liu T, Zhou T, Yao Y, Zhang F, Liu L, Liu Y, et al. Stimulus methods of multi-functional shape memory polymer nanocomposites: a review. Composer Part A Appl Sci Manuf 2017;100:20–30.

[8] Thakur S, Hu J. Polyurethane: a shape memory polymer (smp). Asp. Polyurethanes; 2017. p. 53–71.

[9] Xu J, Song J. Thermal responsive shape memory polymers for biomedical applications. Biomed. Eng. - Front. Challenges 2011:125–42.

[10] Ren L, Li B, Song Z, Liu Q, Ren L, Zhou X. Bioinspired fiber-regulated composite with tunable permanent shape and shape memory properties via 3d magnetic printing. Compos B Eng 2019;164:458–66.

[11] Han MW, Kim MS, Ahn SH. Shape memory textile composites with multi-mode actuations for soft morphing skins. Compos B Eng 2020;198:108170.

[12] Stoychev G, Zakharchenko S, Turcaud S, Dunlop JWC, Ionov L. Shape-programmed folding of stimuli-responsive polymer bilayers. ACS Nano 2012;6:3925–34.

[13] Gracias DH. Stimuli responsive self-folding using thin polymer films. Curr Opin Chem Eng 2013;2:112–9.

[14] Ji S, Wang J, Olah A, Baer E. Triple-shape-memory polymer films created by forced-assembly multilayer coextrusion. J Appl Polym Sci 2017;134:44405.

[15] Ding L, Zhang J, Shu Q, Liu S, Xuan S, Gong X, et al. Magnetism-responsive anisotropic film with self-sensing and multifunctional shape manipulation. ACS Appl Mater Interfaces 2021;13:13724–34.

[16] Wang Q, Liu Z, Tang C, Sun H, Zhu L, Liu Z, et al. Tough interfacial adhesion of bilayer hydrogels with integrated shape memory and elastic properties for controlled shape deformation. ACS Appl Mater Interfaces 2021;13:10457.

[17] Du H, Liu L, Zhang F, Leng J, Liu Y. Triple-shape memory effect in a styrene-based shape memory polymer: characterization, theory and application. Compos B Eng 2019;173:106905.

[18] Aßhoff SJ, Lancia F, Iamsaard S, Matt B, Kudernac T, Fletcher SP, et al. High-power actuation from molecular photoswitches in enantiomerically paired soft springs. Angew Chem Int Ed 2017;56:3261–5.

[19] Yuan C, Ding Z, Wang TJ, Dunn ML, Qi HJ. Shape forming by thermal expansion mismatch and shape memory locking in polymer/elastomer laminates. Smart Mater Struct 2017;26:105027.

[20] Xiao S, Yang Y, Zhong M, Chen H, Zhang Y, Yang J, et al. Salt-responsive bilayer hydrogels with pseudo-double-network structure actuated by polyelectrolyte and antipolyelectrolyte effects. ACS Appl Mater Interfaces 2017;9:20843–51.

[21] Wang W, Xiang C, Zhu Q, Zhong W, Li M, Yan K, et al. Multistimulus responsive actuator with GO and carbon nanotube/PDMS bilayer structure for flexible and smart devices. ACS Appl Mater Interfaces 2018;10:27215–23.

[22] Lu H, Liang F, Yao Y, Gou J, Hui D. Self-assembled multi-layered carbon nanofiber nanopaper for significantly improving electrical actuation of shape memory polymer nanocomposite. Compos B Eng 2014;59:191–5.

[23] Zhang J, Liu X, Zao W, Feng H, Hou Y, Huo A. High-temperature-aging induced sequential recovery of shape memory nitrile butadiene rubber composites. ACS Appl Mater Interfaces 2021;13:10376–87.

[24] Xu W, Jambhulkar S, Zhu Y, Ravichandran D, Kakarla M, Vernon B, et al. 3D printing for polymer/particle-based processing: a review. Compos B Eng 2021;223:109102.

[25] Rao BND, Olajide JL, Sadiku R. 3D printing of fiber reinforced polymer nanocomposites: additive manufacturing. Handb. Nanomater. Nanocomposites Energy Environ. Appl. 2020:1–29. Switzerland: Springer International Publishing.

[26] Xu W, Jambhulkar S, Ravichandran D, Zhu Y, Kakarla M, Nian Q, et al. 3D printing-enabled nanoparticle alignment: a review of mechanisms and applications. Small 2021:2100817.

[27] Ravichandran D, Xu W, Jambhulkar S, Zhu Y, Kakarla M, Bawareth M, et al. Intrinsic field-induced nanoparticle assembly in three-dimensional (3D) printing polymeric composites. ACS Appl Mater Interfaces 2021;13:52274–94.

[28] Xu W, Zhu Y, Ravichandran D, Jambhulkar S, Kakarla M, Bawareth M, et al. Review of fiber-based three-dimensional printing for applications ranging from nanoscale nanoparticle alignment to macroscale patterning. ACS Appl Nano Mater 2021;4:7538–62.

[29] Tao R, Ji L, Li Y, Wan Z, Hu W, Wu W, et al. 4D printed origami metamaterials with tunable compression twist behavior and stress-strain curves. Compos B Eng 2020;201:108344.

[30] Ding Z, Yuan C, Peng X, Wang T, Qi HJ, Dunn ML. Direct 4D printing via active composite materials. Sci Adv 2017;3:e1602890.

[31] Wang W, Yu CY, Abrego Serrano PA, Ahn SH. Soft grasping mechanisms composed of shape memory polymer based self-bending units. Compos B Eng 2019;164:198–204.

[32] Davidson EC, Kotikian A, Li S, Aizenberg J, Lewis JA. 3D printable and reconfigurable liquid crystal elastomers with light-induced shape memory via dynamic bond exchange. Adv Mater 2020;32:1–6.

[33] Mao Y, Yu K, Isakov MS, Wu J, Dunn ML, Jerry Qi H. Sequential self-folding structures by 3D printed digital shape memory polymers. Sci Rep 2015;5:1–12.

[34] Zhou Y, Parker CB, Joshi P, Naskar AK, Glass JT, Cao C. 4D printing of stretchable supercapacitors via hybrid composite materials. Adv Mater Technol 2021;6:2001055.

[35] Joshi S, Rawat K, , C K, Rajamohan V, Mathew AT, Koziol K, et al. 4D printing of materials for the future: opportunities and challenges. Appl Mater Today 2020;18:100490.

[36] Hann SY, Cui H, Nowicki M, Zhang LG. 4D printing soft robotics for biomedical applications. Addit Manuf 2020;36:101567.

[37] Kuang X, Mu Q, Roach DJ, Jerry Qi H. Shape-programmable and healable materials and devices using thermo- and photo-responsive vitrimer. Multifunct Mater 2020;3:045001.

[38] Momeni F, Mehdi Hassani NSM, Liu X, Ni J. A review of 4D printing. Mater Des 2017;122:42–79.

[39] Mitchell A, Lafont U, Hołyńska M, Semprimoschnig C. Additive manufacturing - a review of 4D printing and future applications. Addit Manuf 2018;24:606–26.

[40] Champeau M, Heinze DA, Viana TN, de Souza ER, Chinellato AC, Titotto S. 4D printing of hydrogels: a review. Adv Funct Mater 2020;30:1910606.

[41] Singh S, Ramakrishna S, Berto F. 3D Printing of polymer composites: a short review. Mater Des Process Commun 2020;2:97–109.

[42] Ravichandran D, Xu W, Kakarla M, Jambulkar S, Zhu Y, Song K. Multiphase direct ink writing (MDIW) for multilayered polymer/nanoparticle composites. Addit Manuf 2021;47:102322.

[43] Schrenk Wj T. Alfrey J. Coextruded Multilayer Polymer Films and Sheets. Polym. Blends 1978;2:129–65.

[44] Lau K tak, Gu C, Hui D. A critical review on nanotube and nanotube/nanoclay related polymer composite materials. Compos B Eng 2006;37:425–36.

[45] Safri SNA, Sultan MTH, Jawaid M, Jayakrishna K. Impact behaviour of hybrid composites for structural applications: a review. Compos B Eng 2018;133:112–21.

[46] Sisson AL, Ekinci D, Lendlein A. The contemporary role of ε-caprolactone chemistry to create advanced polymer architectures. Polymer 2013;54:4333–50.

[47] Guo Y, Yan L, Zeng Z, Chen L, Ma M, Luo R, et al. TPU/PLA nanocomposites with improved mechanical and shape memory properties fabricated via phase morphology control and incorporation of multi-walled carbon nanotubes nanofillers. Polym Eng Sci 2020;60:1118–28.

[48] Xu W, Ravichandran D, Jambhulkar S, Zhu Y, Song K. Hierarchically structured composite fibers for real nanoscale manipulation of carbon nanotubes. Adv Funct Mater 2021;31:2009311.

[49] Xu W, Jambhulkar S, Verma R, Franklin R, Ravichandran D, Song K. In situ alignment of graphene nanoplatelets in poly(vinyl alcohol) nanocomposite fibers with controlled stepwise interfacial exfoliation. Nanoscale Adv 2019;1:2510–7.

[50] Mahmud MB, Anstey A, Shaayegan V, Lee PC, Park CB. Enhancing the mechanical performance of PA6 based composites by altering their crystallization and rheological behavior via in-situ generated PPS nanofibrils. Compos B Eng 2020;195:108067.

[51] Kim BK, Lee SY, Xu M. Polyurethanes having shape memory effects. Polymer 1996;37:5781–93.

[52] Zhao W, Liu L, Leng J, Liu Y. Thermo-mechanical behavior prediction of particulate reinforced shape memory polymer composite. Compos B Eng 2019;179:107455.

[53] Zhao Q, Zou W, Luo Y, Xie T. Shape memory polymer network with thermally distinct elasticity and plasticity. Sci Adv 2016;2:e1501297.

[54] Taguchi R, Akamatsu N, Kuwahara K, Tokumitsu K, Kobayashi Y, Kishino M, et al. Nanoscale Analysis of surface bending strain in film substrates for preventing fracture in flexible electronic devices. Adv Mater Interfac 2021;8:2001662.

[55] Kim TW, Lee JS, Kim YC, Joo YC, Kim BJ. Bending strain and bending fatigue lifetime of flexible metal electrodes on polymer substrates. Materials 2019;12:2490.

[56] Xin C, Jin D, Hu Y, Yang L, Li R, Wang L, et al. Environmentally adaptive shape-morphing microrobots for localized cancer cell treatment. ACS Nano 2021;15:18048–59.

[57] Xu T, Zhang J, Salehizadeh M, Onaizah O, Diller E. Millimeter-scale flexible robots with programmable three-dimensional magnetization and motions. Sci Robot 2019;4:eaav4494.

[58] Hu W, Lum GZ, Mastrangeli M, Sitti M. Small-scale soft-bodied robot with multimodal locomotion. Nature 2018;554:81–5.

[59] Kim Y, Yuk H, Zhao R, Chester SA, Zhao X. Printing ferromagnetic domains for untethered fast-transforming soft materials. Nature 2018;558:274–9.

[60] Hu X, Ge Z, Wang X, Jiao N, Tung S, Liu L. Multifunctional thermo-magnetically actuated hybrid soft millirobot based on 4D printing. Compos B Eng 2022;228:109451.

[61] Lee TD, Ebong AU. A review of thin film solar cell technologies and challenges. Renew Sustain Energy Rev 2017;70:1286–97.

[62] Hołyńska M, Tighe A, Semprimoschnig C. Coatings and thin films for spacecraft thermo-optical and related functional applications. Adv Mater Interfac 2018;5:1701644.

[63] Kang S, Kang TH, Kim BS, Oh J, Park S, Choi IS, et al. 2D reentrant micro-honeycomb structure of graphene-CNT in polyurethane: high stretchability, superior electrical/thermal conductivity, and improved shape memory properties. Compos B Eng 2019;162:580–8.

[64] Farouki RT, Han CY, Manni C, Sestini A. Characterization and construction of helical polynomial space curves. J Comput Appl Math 2004;162:365–92.

[65] Olsen K, Bohr J. Geometry of the toroidal N-helix: optimal-packing and zero-twist. New J Phys 2012;14:023063.

[66] Olsen K, Bohr J. The generic geometry of helices and their close-packed structures. Theor Chem Acc 2010;125:207–15.

[67] Ze Q, Kuang X, Wu S, Wong J, Montgomery SM, Zhang R, et al. Magnetic shape memory polymers with integrated multifunctional shape manipulation. Adv Mater 2020;32:1906657.

[68] Wei H, Zhang Q, Yao Y, Liu L, Liu Y, Leng J. Direct-write fabrication of 4D active shape-changing structures based on a shape memory polymer and its nanocomposite. ACS Appl Mater Interfaces 2017;9:876–83.

[69] Lemine OM. Magnetic hyperthermia therapy using hybrid magnetic nanostructures. Hybrid Nanostructures for Cancer Theranostics 2018:1–10. Elsevier Inc.

[70] Stephen ZR, Kievit FM, Zhang M. Magnetite nanoparticles for medical MR imaging. Mater Today 2011;14:330–80.

[71] Lorkowski ME, Atukorale PU, Ghaghada KB, Karathanasis E. Stimuli-responsive iron oxide nanotheranostics: a versatile and powerful approach for cancer therapy. Adv Healthc Mater 2021;10:2001044.